

Mechanisms for diffusion-driven growth of cavitating wing-tip vortices

Nanda, Swaraj; Westerweel, Jerry; van Terwisga, Tom; Elsinga, Gerrit

DOI

[10.1016/j.ijmultiphaseflow.2022.104146](https://doi.org/10.1016/j.ijmultiphaseflow.2022.104146)

Publication date

2022

Document Version

Final published version

Published in

International Journal of Multiphase Flow

Citation (APA)

Nanda, S., Westerweel, J., van Terwisga, T., & Elsinga, G. (2022). Mechanisms for diffusion-driven growth of cavitating wing-tip vortices. *International Journal of Multiphase Flow*, 156, Article 104146. <https://doi.org/10.1016/j.ijmultiphaseflow.2022.104146>

Important note

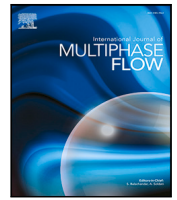
To cite this publication, please use the final published version (if applicable). Please check the document version above.

Copyright

Other than for strictly personal use, it is not permitted to download, forward or distribute the text or part of it, without the consent of the author(s) and/or copyright holder(s), unless the work is under an open content license such as Creative Commons.

Takedown policy

Please contact us and provide details if you believe this document breaches copyrights. We will remove access to the work immediately and investigate your claim.



Mechanisms for diffusion-driven growth of cavitating wing-tip vortices

Swaraj Nanda^{a,*}, Jerry Westerweel^a, Tom van Terwisga^{b,c}, Gerrit Elsinga^a

^a Laboratory for Aero and Hydrodynamics, Delft University of Technology, The Netherlands

^b Maritime Research Institute of the Netherlands (MARIN), The Netherlands

^c Ship Hydromechanics and Structures, Delft University of Technology, The Netherlands

ARTICLE INFO

Keywords:

Vortex cavitation
Dissolved gas
Diffusion modeling

ABSTRACT

Following their inception, vortex cavities emanating from stationary wing tips in cavitation tunnels are often observed to grow. These effects are usually attributed to the free and dissolved non-condensable gases in the liquid. However, a detailed mechanism for the cavity's growth is not known. Consequently, the repeatability of vortex cavitation in different flow facilities is generally poor. The main aim of our work is to highlight the contribution of dissolved gases to the cavity's growth, hence addressing water-quality influence in nuclei-depleted conditions. A model is provided for a steady-state diffusion-driven mechanism that transports dissolved gases from the surrounding liquid into the vortex cavitation through a diffusion layer located outside its interface. The model results show that the cavity grows uncontrollably when the dissolved gas concentration in the liquid is saturated or oversaturated relative to its saturation level at ambient pressure conditions ($c_{\infty}/c_{sat} \geq 1$). In addition, it is shown that stable cavity sizes can be achieved when the $c_{\infty}/c_{sat} < 1$. The predictions in the range $1.04 \leq c_{\infty}/c_{sat} \leq 1.33$ are compared with experimental data and infer either of the two geometries for the diffusion layer: (i) a 5 μm thin film approximated by a hollow cylinder around the cavity, or (ii) one that evolves like a boundary layer along the axis of the cavity. For the latter modeling approach, the observed length of the cavity was much larger than that required to match with the experimental data, skewing a preference to the thin-film assumption. In the undersaturated regime ($c_{\infty}/c_{sat} = 0.14$ & 0.39), the proposed model has a qualitative agreement with the data of Briançon-Marjollet and Merle (1996).

1. Introduction

Tip Vortex-cavitation is a form of hydrodynamic cavitation that initiates when the low-pressure core of the vortex shed by a lifting-body approaches the local vapor pressure of water (Arndt, 2002; Brennen, 2014; Cheng et al., 2021), resulting in the formation of dynamic vapor-liquid structures. An important feature of vortex-cavitation stems from the dynamics of its interface (Pennings et al., 2015) that causes a fluctuating pressure field in its surrounding, acting as a source of fatigue load to the hull structure, as well as a source of sub-kilohertz, tonal, radiated noise into the underwater environment (Bosschers, 2018b). The resulting disruption to the global marine habitat has been reported by various studies (Jones, 2019; Duarte et al., 2021), and, this phenomenon has been studied extensively by conducting observations in cavitation tunnels (Holl et al., 1972; Higuchi et al., 1989; Arndt et al., 1991; van Wijngaarden et al., 2005). One point of contention is that cavitation facilities vary one from another, sometimes in the volumetric water capacity of the tunnel, or the achievable Reynolds and cavitation number of the flow. More importantly, cavitation tunnels vary in their ability to control the water quality content, here identified

by the amount of free gas bubbles, or nuclei, and gases dissolved within the fluid. As a result, repeatability of cavitation observations across facilities is often poor (Atlar, 2002).

In the case of vortex cavitation inception, water-quality effects are largely dominated by the distribution of nuclei bubbles in the flow (McCormick, 1962; Arndt and Keller, 1992; Arndt and Maines, 2000; Khoo et al., 2020). However, immediately following inception when the cavity is saturated with water vapor at its vapor pressure, a higher concentration of dissolved-air in the liquid adjacent to its boundary will initiate a mass-transfer process across the boundary, causing the pressure inside the vortex cavity to increase. The resulting vaporous cavitation will transition to gaseous cavitation, and due to continued mass transfer of gases into the cavity, the cavity radius will increase over time. In order to terminate this growth process, the concentration difference across the vapor-liquid boundary should be bridged. But how long is this development period? What is the rate at which this development occurs and what are the physical quantities most important to this phenomenon? Under what conditions does a vortex cavity achieve a stable size? Answers to these questions are

* Corresponding author.

E-mail address: swaraj.nanda.2019@gmail.com (S. Nanda).

unclear. Clearly, a phenomenological picture of the stability of a vortex cavity size following inception, as influenced by water quality effects, is necessary. In the present work, we separate the influence of the nuclei content in the flow by considering only those cases where the nuclei population in the flow is low enough to be inconsequential to our observations.

1.1. Related works on dissolved gas diffusion modeling

One of the first theoretical models on the mass transfer of dissolved gases into bubbles was developed by Epstein and Plesset (1950). They studied the growth and dissolution of microbubbles theoretically by assuming that the gas concentration in the bubble and on its surface are saturated relative to its internal pressure. The mass-transfer mechanism is approximated as an unsteady diffusion process analogous to heat conduction in spheres. This is used to estimate a radial concentration profile which ultimately equalizes with the ambient dissolved gas concentration far away from the bubble interface. They also considered the influence of surface tension by incorporating the pressure balance at the interface, and their predictions are in good agreement with dissolution times observed for microbubble radii less than 15 μm and a surface tension range of 25 to 72 mN/m (Duncan and Needham, 2004).

In contrast to gas diffusion in stationary bubbles, hydrodynamic cavitation often occurs in the vicinity of high flow velocities, where convective components cannot be readily ignored and Peclet numbers are high. In this regard, a convective diffusion mechanism was proposed by Van Wijngaarden (1967) for microbubble growth rates observed in the wakes of flow-facing objects by Kermeen and McGraw (1952). The convective diffusion modeling approach has also been useful in describing the growth and shedding of microbubble nuclei from gas pockets attached to surface crevices (Groß and Pelz, 2017). In this case and the prior case, where the microbubble is embedded in a turbulent flow, the relative motion of the surrounding flow to the interface indeed merits the inclusion of a convective component in the growth mechanism. Yet another bubble growth mechanism is rectified diffusion (Eller and Flynn, 1965; Fyrrillas and Szeri, 1994) which accounts for the non-linear mass transfer of air across a bubble interface induced by an oscillating boundary. This modeling approach may be relevant to the vortex cavity whose interface dynamics could act as a non-linear mass transfer component. While this is a consideration, the diffusion layer morphology for this flow problem is yet to be established and will be elaborated in Section 1.2.

Gas diffusion is also known to affect cavitation phenomenon in larger scales as well. Holl and Treaster (1966) connected the presence of dissolved gases to cavitation hysteresis observed in large developed cavities generated behind flow facing objects (Holl, 1960; Gadd and Grant, 1965) and Brennen (1969) proposed the first mass transfer model for the diffusion of dissolved gases into large axisymmetric cavities. In this model, the mass transfer mechanism was approximated as a two-dimensional, steady state, convective diffusion mechanism occurring over a potential flow background. However, an extension of this solution to three-dimensional cavities by wrapping the two-dimensional model around the cavity, as done by Billet and Weir (1975), over-predicted the observed growth rate by one order of magnitude. Parkin and Ravindra (1991) tried to resolve the discrepancy by adopting a turbulent diffusivity obtained from a mixing-length model and showed that the mass-transfer region that contributes to the most mass-flux resides near the frontal region of the cavity, where the concentration gradient at the surface has the highest magnitude. They also showed that a wrap-around solution closely approaches an axisymmetric solution with acceptable loss of accuracy.

More recently, Yu and Ceccio (1997) and Lee et al. (2016) applied the available convective-diffusion models to limited partial cavities (Holl et al., 1972), observed using X-ray measurements. They found the proposed models (Brennen, 1969; Billet and Weir, 1975; Parkin and Ravindra, 1991) to be ineffective in predicting the bubbles sizes left in

its wake. Surprisingly, they were able to scale the order-of-magnitude of growth rates observed by assuming a cumulative molecular diffusion (following Epstein and Plesset (1950)) into an assumed monodisperse population of the average microbubble size within the partial cavity. To us, the result reaffirms the role of molecular diffusion in the mass transfer of dissolved gases into bubbles. In the following discussion, we try to motivate the role of molecular diffusion for vortex cavities as well.

1.2. Related works for vortex cavitation flows

In contrast to the experimental and theoretical works present for nucleation and partial cavitation, literature on vortex cavitation growth and development due to dissolved gases in its surrounding is not extensive. Some reasons for this could be the following: (1) Cavitation tunnels water quality management is non-standardized across facilities; (2) Vortex cavitation sound has a greater emphasis than water quality sensitivity, whose high frequency dynamics lead to a small observation duration, typically of $\mathcal{O}(1)$ seconds; and, (3) Experimentation practices for generating the vortex cavity are not adequately described. In order to allow the cavity to develop, or grow, to a quasi-stable size, it is common to have an arbitrary buffer time between inception and observation (Dreyer et al., 2014; Pennings et al., 2014; Amini et al., 2019). In the absence of a standardized measurement practice, where the exposure time of the vortex cavity to its surroundings is categorized and its influence is understood, the observer is likely to perceive a slowly developing cavity to be stable. This introduces observer specific biases into the measurements.

To the best of our knowledge, long-time observations of the size of vortex-cavities have only been reported by Briançon-Marjollet and Merle (1996) for their measurements at the GTH facility (Lecoffre et al., 1988), indeed showing a growing vortex cavity radius following its inception. In some of these measurements, the water-tunnel was operated in nuclei-depleted conditions, still showing an appreciable growth rate of the vortex cavity size. Table 1 reproduces some of their measurements by calculating the change in cavity radius (Δr) over its growth duration (Δt), characterized using the non-dimensional mass-transfer Fourier number F_m . Here $F_m = \Delta t D / (\Delta r_c)^2$, where D is binary diffusion coefficient for the solute-solvent configuration, here air-water. The mass Fourier number as defined here compares the magnitude of the growth rate of the cavity in a given period with the molecular diffusion for that gas-liquid configuration, with a value approaching $\mathcal{O}(1)$ identified as a strongly diffusion dominated phenomenon.

For some cases in Table 1, it is observed that a flow where the nuclei population is moderate to none results in a F_m value only one order of magnitude below $\mathcal{O}(1)$ indicating that the growth mechanism could be diffusion driven. At the same time, one also observes that an increased presence of nuclei-content increases the growth rate, leading to smaller F_m values. This suggests that the growth rate of a cavitating vortex may be sensitive to large nuclei population density in the water-tunnel. However, besides establishing an order-of-magnitude wise connection to molecular diffusion, conclusions made on the effect of the ambient relative air-saturation level (c_∞/c_{sat}) to the growth rate are limited. Here, c_∞ is the ambient air-concentration with units of density, while c_{sat} is the air-concentration of the fully saturation solution at the tunnel's ambient pressure conditions.

Numerical simulations of vortex-cavitation typically do not consider the influence of dissolved gases for the slow growth rates attributed to them. Instead, Euler-Lagrangian models of nuclei entrainment as a mechanism for the growth of vortex-cavities has been considered in a recent numerical work by Cheng et al. (2020). The modeling involves a modification of the Schnerr-Sauer cavitation model (Schnerr and Sauer, 2001), assuming the presence of non-condensable gas as a monodisperse spherical bubble population, disregarding the influence of dissolved air entirely. Theoretical work on the entrainment of nuclei into vortices has been considered by, for example, Zhang et al. (2017),

Table 1

Estimates of F_m from data found in Briançon-Marjollet and Merle (1996). σ is the reported cavitation number, U_∞ is the reported inflow velocity and p_∞ is the ambient pressure estimated using a vapor pressure of 2 kPa and water density of 1 g/cm³. The relative saturation level (c_∞/c_{sat}) is reported relative to saturation conditions c_{sat} at the estimated test section pressure p_∞ . c_{sat} is calculated from the estimated ambient pressure and using Henry's law with Henry's constant for air being 0.223×10^{-6} kg/m³ Pa. The binary diffusion constant is taken to be 2×10^{-9} m²/s.

	σ [-]	U_∞ [m/s]	p_∞ [$\times 10^5$ Pa]	Dissolved-air [% a.s. re 1 atm]	c_∞/c_{sat} [-]	Nuclei-Seeding [-]	Δt [s]	Δr_c [mm]	F_m [-]
1	4.1	10	2.07	30	0.14	Large nuclei	1548	10.30	0.03
2	4.1	10	2.07	80	0.39	No seeding	332	3.39	0.26
3	2.9	6	0.54	30	0.56	No seeding	590	1.73	0.40
4	2.9	6	0.54	30	0.56	Small nuclei	1374	3.98	0.17

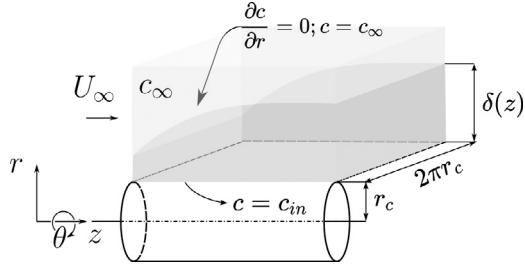


Fig. 1. A schematic description of the convective-diffusion model found in Amini et al. (2019). c_{in} is the concentration of air at the cavity interface on the vapor-side and c_∞ is the dissolved air content in the ambient liquid. The region where the concentration gradient develops is marked as dark gray, where $\delta(z)$ refers to the concentration boundary layer thickness along the axial direction, and $\delta(z) \ll r_c$. The unwrapped tangential coordinate is depicted as a planar three-dimensional extrusion over a length $2\pi r_c$.

Oweis et al. (2005), and more recently by Chen et al. (2019). When the number of free gas bubbles is strongly reduced, one can consider that the mass flow rate of gas into the cavity by nuclei entrainment is negligible compared to that by diffusion. From our discussion of the results of Briançon-Marjollet and Merle (1996), it is clear that gas-diffusion is important to vortex-cavitation phenomenon, particularly in nuclei depleted conditions. While the influence of dissolved gases on the growth rate and stability of the cavity size remains unknown to this present date, there has been an attempt to model the growth rate of a tip-vortex cavity using the convective-diffusion approach.

Recently, Amini et al. (2019) have proposed a convective-diffusion mechanism (see Fig. 1) using the two-dimensional potential-flow diffusion model discussed by Brennen (1969). In this approach, the governing transport equation for the single species dissolved gas-concentration, c (with units of density), given by:

$$\left[\frac{\partial c}{\partial t} \right]_I + [u \cdot (\nabla c)]_{II} = [D \nabla^2 c]_{III} \quad (1)$$

can be simplified considering (i) two-dimensionality in a cartesian frame, (ii) no accumulation of mass in the diffusion layer (negligible term I of Eq. (1)), (iii) negligible radial velocity of the cavity, (iv) axisymmetry, and, (v) no axial diffusion component given that the Peclet number is large. $Pe = U_\infty l_c / D$, where U_∞ is the axial flow speed, and l_c the length of a section of the vortex cavity. This gives:

$$U_\infty \frac{\partial c}{\partial z} \approx D \frac{\partial^2 c}{\partial r^2}. \quad (2)$$

Over the length of the cavity, the radial concentration profile of dissolved gas is assumed to evolve in a self-similar manner. The two-dimensional solution is wrapped around a cylindrical geometry with negligible loss of accuracy compared to a fully axisymmetric model as shown by Parkin and Ravindra (1991). The resulting total mass-transfer rate of gas into a longitudinal segment of the cavity, \dot{m} , is then derived by Amini et al. (2019) as:

$$\dot{m}_{CD} \approx 4r_c(c_\infty - c_{in})\sqrt{\pi U_\infty D l_c}. \quad (3)$$

One missing aspect of Eq. (3) is its connection to the increasing total pressure inside the cavity. This is because, if a *quasi-steady* growth-behavior as motivated by the observations of Briançon-Marjollet and

Merle (1996) and those reported here (see Section 3) is assumed, an interfacial pressure balance of the following form must be obeyed during the growth stage:

$$[p_{in}^G(t) + p_{vap}]_c = [p_\infty + p_c(r_c)] + p_T(r_c) \quad (4)$$

where p_{in}^G is the time-dependent pressure of air inside the cavity, p_{vap} the vapor pressure of water, p_∞ the ambient pressure, p_c the radial pressure distribution of the vortex relative to p_∞ , and p_T the contribution of surface tension due to curvature in circumferential direction. One uncertainty with combining the mass-transfer rate of Eq. (3) with the pressure balance across the interface Eq. (4) is that the concentration profile inside the cavity is unknown and must be assumed. Secondly, within an analytical or semi-empirical framework, the radial-pressure at the interface, $p_c(r_c)$, requires a vortex-model that is suited to cavitating flows. Therefore, one is not sure if the potential flow convective-diffusion approach yielding Eq. (3) is the only mechanism that describes diffusion driven growth of the vortex cavity.

To tackle the challenge of scaling the size of a vortex cavity using the dissolved gas content, the flow Reynolds number and cavitation number, it is first important to understand how gas is transported into the cavity from dissolved gas present in its surrounding. In this work, we propose that this mechanism is strongly diffusion driven. We approximate the wing-tip vortex cavity as a line vortex and apply different modeling assumptions to arrive at an estimate of the cavity growth rate, which we compare with experiments. We generate the cavitating tip-vortex using a NACA 66₂-415 elliptical foil, similar to Pennings (2016) and conduct long-time observations (> 5 min) of the development phase of a vortex cavity.

1.3. Outline

We structure our paper as follows: In Section 2 of this work, we examine the potential-flow convective-diffusion mass transfer approach to vortex cavity growth rates, and, propose additional mass-transfer mechanisms for the same. We also connect these mass-transfer rates to the growth rate of the cavity by incorporating the *quasi-steady* pressure-balance at the cavity's interface (Eq. (4)). In Section 3 our experimental investigation is detailed where a special emphasis is placed on the measurement procedure to obtain repeatable results in a low-volume cavitation tunnel. Our experimental results, compared with the different growth rate models, are highlighted and discussed in Section 4. The paper then closes with the conclusion in Section 5.

2. Modeling

In all our modeling attempts, we assume that the mass-transfer rate estimated at the liquid side of the interface results in a uniform growth in the cavity-radius along its length. The assumption of uniform cavity growth is motivated primarily by our own experimental observations, discussed later in Section 3.1 and in Fig. 4. In Section 2.1, we use this assumption in the estimation of the growth-rate of the cavity radius, which is equated to three different mass-transfer models that we describe in Section 2.2, with one of the models being the convective-diffusion model used by Amini et al. (2019). Some distinguishing features of the mass-transfer models are described in Section 2.2.4, and

finally some comments on the choice of different vortex-models in the growth-rate expressions are given in Section 2.2.5.

The modeling has been performed for conditions following inception of the vortex cavity, and before the eventual unstable state observed in each cavitation measurement in oversaturated conditions, later described in Fig. 4 and its accompanying discussion. In this growth period, the primary assumption made is that the radial velocity of the cavity interface is negligible relative to the expected azimuthal velocity of the fluid in its vicinity. Therefore, we consider the growth behavior to be quasi-steady.

2.1. Cavity growth rate expression for purely radial growth in size

Consider the vortex cavity as a cylinder of constant length l_c , ignoring the endcaps and with radius $r_c(t)$. As the circulation is proportional to the lift generated by the wing, which does not change during the measurements, the ambient circulation strength of the vortex, Γ_∞ , is taken constant. Assuming that the transported gas is ideal and in isothermal conditions, then, for any temperature T , where M_G is the molecular mass and R the ideal gas constant, the density $\rho_{in}^G(t)$ equals $p_{in}^G(t)M_G/RT$. This can be substituted into the pressure balance expression of Eq. (4) as follows:

$$\rho_{in}^G(t) = \tau \{p_\infty + p_c(r_c) + p_T(r_c) - p_{vap}\} \quad (5)$$

where $\tau = M_G/RT$. Furthermore, the mass of the gas contained inside a cavity of length l_c is given by:

$$m_{in}^G = (\pi r_c^2) \rho_{in}^G(t) l_c \quad (6)$$

Taking the time derivative of Eq. (6), the mass-transfer rate per unit length of the cavity is given by the following expression:

$$\begin{aligned} \frac{1}{l_c} \frac{dm_{in}^G}{dt} &= \frac{d}{dt} [(\pi r_c^2) \rho_{in}^G(t)] \\ &= 2\pi r_c \rho_{in}^G(t) \frac{dr_c}{dt} + \pi r_c^2 \frac{d\rho_{in}^G(t)}{dt} \end{aligned} \quad (7)$$

The term $d\rho_{in}^G(t)/dt$ contains $p_c(r_c)$ and $p_T(r_c)$ which is expanded using the chain rule and substituted into Eq. (7), yielding:

$$\frac{1}{l_c} \frac{dm_{in}^G}{dt} = 2\pi r_c \frac{dr_c}{dt} \left[\rho_{in}^G(t) + \frac{\tau r_c}{2} \left(\frac{dp_T}{dr_c} + \frac{dp_c}{dr_c} \right) \right] \quad (8)$$

Eq. (8) gives the rate of change in mass of gas inside the cavity which can then be equated to a mass-transfer model. For a purely radial diffusion, the mass introduced into the cavity per unit length and per unit time is given by the expression:

$$\frac{1}{l_c} \frac{dm_{in}^G}{dt} = 2\pi r_c D \left(\frac{\partial c}{\partial r} \right)_{r_c} \quad (9)$$

Here, D is the binary diffusion coefficient between liquid and gas while $(\partial c/\partial r)_{r_c}$ is the concentration gradient at the cavity interface. From Eqs. (8) and (9), we have:

$$2\pi r_c D \left(\frac{\partial c}{\partial r} \right)_{r_c} = 2\pi r_c \frac{dr_c}{dt} \left[\rho_{in}^G(t) + \frac{\tau r_c}{2} \left(\frac{dp_T}{dr_c} + \frac{dp_c}{dr_c} \right) \right].$$

Finally, the above is rearranged to yield the expression for cavity growth rate due to diffusion of ambient dissolved gases into the cavity:

$$\frac{dr_c}{dt} = \frac{D \left(\frac{\partial c}{\partial r} \right)_{r_c}}{\left[\rho_{in}^G(t) + \frac{\tau r_c}{2} \left(\frac{dp_T}{dr_c} + \frac{dp_c}{dr_c} \right) \right]}. \quad (10)$$

Eq. (10) is a first-order differential equation describing the cavity growth rate, requiring the modeling of mass-transfer through the $(\partial c/\partial r)_{r_c}$ term and a vortex-model for the pressure gradient term $(\partial p_c/\partial r_c)$.

2.2. Mass-transfer modeling

2.2.1. Mass-transfer considering a convective-diffusion process

As described by Amini et al. (2019), the convective-diffusion model takes a two-dimensional, cartesian representation of Eq. (1) in the axial and radial direction, assumes a steady-state diffusion process, negligible radial velocity, axial velocity equal to freestream, a large Peclet number, and a self similarly evolving concentration profile in the diffusion layer that scales with $\sqrt{Dz/U_\infty}$ as shown in Fig. 1. These approximations reduce the concentration transport equation to Eq. (2). The expression for the mass-transfer rate of dissolved-gas into the cavity, neglecting the end-caps of the cylinder, is obtained by integrating the local mass-transfer rate per unit area over its length, l_c , yielding a mass-transfer rate given by Eq. (3). In order to derive a growth rate expression for a developing cavity using the convective-diffusion approach, the mass-transfer rate in Eq. (3) can be substituted to Eq. (8) to yield the following approximate first-order ordinary differential equation:

$$\frac{dr_c}{dt} = \frac{(c_\infty - c_{in})}{\left[\rho_{in}^G(t) + \frac{\tau r_c}{2} \left(\frac{dp_T}{dr_c} + \frac{dp_c}{dr_c} \right) \right]} \left[\sqrt{\frac{4DU_\infty}{\pi l_c}} \right]_{U_D^{cd}} \quad (11)$$

The component of Eq. (11) highlighted by subscript U_D^{cd} has the units of velocity and scales with the diffusion velocity of dissolved gas across the interface. We make this distinction for the explicit purpose of comparing the behavior of the diffusion model discussed here, in Section 2.2.3 and in Section 2.2.2. We revisit this diffusion velocity term in Section 2.2.4 and in the results section, Section 4. Likewise, the denominator of Eq. (11) excluding U_D^{cd} has units of density and can be thought to scale with the density of the gas molecules at the interface location. This is governed by the balance between partial gas-pressure inside the cavity, the dynamic pressure at the interface described by a vortex-model and a surface-tension component due to curvature in the azimuthal direction alone.

2.2.2. Mass-transfer through a thin diffusion-layer approximated as a hollow cylinder

If the diffusion layer has no relative motion with respect to the surrounding flow, the radial velocity is negligible, the transport is steady and axisymmetric and the diffusion layer has a constant thickness δ_f along its length, with the condition that $r_c \gg \delta_f$ (see Fig. 2), then Eq. (1) is reduced to:

$$\frac{D}{r} \frac{\partial}{\partial r} \left(r \frac{\partial c}{\partial r} \right) \approx 0. \quad (12)$$

In this case, the diffusion coefficient would be that of air in water. In order to obtain solutions to the above equation, the concentration field on either side of the diffusion film is assumed to be uniform along both the axial and radial direction. If the measured concentration of dissolved gas (G) in the liquid outside the diffusion layer is given by c_∞ , and, the concentration on the inner wall of the layer is given by c_{in} which increases with time, the solution to Eq. (12) is analogous to that of heat flux through hollow infinite cylinders. Then, the concentration profile inside the cavity interface ($c(r)$) is given by the steady-state analytical solution (see Crank (1979)):

$$c(r) = \left(\ln \left(1 + \frac{\delta_f}{r_c} \right) \right)^{-1} \left[c_\infty \ln \left(\frac{r}{r_c} \right) + c_{in} \ln \left(\frac{r_c + \delta_f}{r} \right) \right]; r \in [r_c, r_c + \delta_f] \quad (13)$$

which gives us the concentration-gradient at the inner wall of the diffusion film:

$$\left(\frac{\partial c}{\partial r} \right)_{r_c} = \frac{1}{r_c} (c_\infty - c_{in}) \left(\ln \left(1 + \frac{\delta_f}{r_c} \right) \right)^{-1}. \quad (14)$$

Finally, substitution of Eq. (14) into Eq. (10) results in:

$$\frac{dr_c}{dt} = \frac{c_\infty - c_{in}}{\left[\rho_{in}^G(t) + \frac{\tau r_c}{2} \left(\frac{dp_T}{dr_c} + \frac{dp_c}{dr_c} \right) \right]} \left[\frac{D}{r_c} \left(\ln \left(1 + \frac{\delta_f}{r_c} \right) \right)^{-1} \right]_{U_D^{cf}}, \quad (15)$$

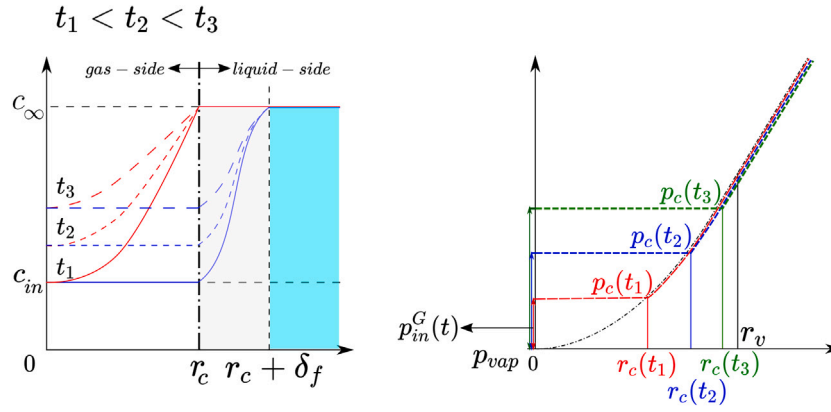


Fig. 2. Left: A schematic description of the diffusion models described in Section 2.2.3 (red) and Section 2.2.2 (blue), c_∞ is the dissolved air content in the ambient liquid and c_{in} refers to the internal concentration profile in the gas-side. The figure also describes the evolving concentration profile within the diffusion layer of each model, highlighting their differences. Right: A schematic describing the radial pressure distribution from the cavity center onward, during its growth, ignoring the interfacial pressure jump due to surface tension. The flat-line profile of the pressure distribution inside the cavity represents homogeneity of gas content inside. (For interpretation of the references to color in this figure legend, the reader is referred to the web version of this article.)

where, U_D^{lf} scales with the diffusion velocity of the dissolved gas at the cavity surface. While this appears to be a function of the cavity radius, the above expression can be simplified by considering a Taylor expansion of the term $\ln(1 + \delta_f/r_c)$, to the first order, considering $\delta_f/r_c \ll 1$. This gives the following approximation to U_D^{lf} :

$$U_D^{lf} \approx D/\delta_f \quad (16)$$

2.2.3. Heat-conduction analogue

In similar fashion as Epstein and Plesset (1950), one may assume the diffusion mechanism to be transient. The concentration profile outside the cavity radius is assumed to be uniform, and the radial distance from the cavity axis to the interface is the region that contains the concentration gradient. Therefore, the concentration gradient at the interface decides the mass-transfer rate. In contrast to the models introduced previously, the location of the diffusion region is inside the cavity, which necessitates an unsteady state mass-transfer process because mass accumulation within the cavity must be considered. If the internal concentration profile is assumed to be axisymmetric, axially invariant, and, convection is ignored in a manner similar to 2.2.2, Eq. (1) simplifies to:

$$\frac{\partial c}{\partial t} \approx \tilde{D} \frac{\partial^2 c}{\partial r^2} \quad (17)$$

If r^+ represents the normalized internal radial position (r/r_c), $c^+ (1 - c(r)/c_\infty)$ represents the normalized internal radial concentration deficit relative to interface conditions, and, t^+ representing the normalized-time step as a Fourier number ($t\tilde{D}/r_c(t)^2$), we require an initial and boundary condition to derive an analytical estimate of c^+ . \tilde{D} represents the diffusion coefficient of air in water-vapor, instead of air in water, as was the case in Sections 2.2.1 and 2.2.2. This distinction is a consequence of the diffusion layer being inside the vortex cavity.

If at the interface ($r^+ = 1$), the concentration remains constant and equal to c_∞ , i.e., $c^+ = 0$ at $r^+ = 1 \forall t^+$, $\partial c^+/\partial r^+(r^+ = 0) = 0$ due to the axisymmetry assumption, and finally, if no gas is present inside the cavity on inception, i.e., $c^+ = 1 \forall r^+ \in [0, 1)$ at $t^+ = 0$, the normalized form of the equation is similar to transient, axisymmetric, heat conduction into solid cylinders. This allows borrowing the analytical solution of c^+ (Cussler, 2009):

$$c^+(t^+, r^+) = \sum_{n=1}^{\infty} \left[\frac{2}{\alpha_n J_1(\alpha_n)} \right] J_0(\alpha_n r^+) e^{-\alpha_n^2 t^+}, \quad (18)$$

where, J_0 and J_1 are the zeroth and first order Bessel function of the first kind. α_n represents an infinite set of positively valued numbers

for which $J_0(\alpha_n) = 0$, or, the zero crossings of the zeroth order of J .¹ We note here that the analytical solution is for constant cavity radius, therefore, the model described in this section is an approximation.

In order to obtain the interfacial concentration gradient, the derivative of Eq. (18) w.r.t. r^+ can be expanded using chain-rule which finally yields the concentration gradient at the interface in non-normalized form:

$$\left(\frac{\partial c}{\partial r} \right)_{r_c} = \frac{2c_\infty}{r_c} \sum_{n=1}^{\infty} \exp\left(\frac{-\alpha_n^2 t \tilde{D}}{r_c^2} \right). \quad (19)$$

Eq. (19) can be substituted into Eq. (10) to give a growth rate formulation for the cavity size:

$$\frac{dr_c}{dt} = \frac{c_\infty}{\left[\rho_{in}^G(t) + \frac{\tau r_c}{2} \left(\frac{dp_r}{dr_c} + \frac{dp_c}{dr_c} \right) \right]} \left[\frac{2\tilde{D} \sum_{n=1}^{\infty} \exp\left(\frac{-\alpha_n^2 t \tilde{D}}{r_c^2} \right)}{r_c} \right]_{U_D^{ma}}, \quad (20)$$

where, U_D^{ma} scales with the diffusion velocity of the dissolved gas at the interface. One issue that arises from the model is that, as incipient cavities are much thinner than a developed cavity, the model might predict a rapid vanishing concentration gradient at the interface following inception.

2.2.4. Comparison between mass-transfer approaches

There are two main type of differences that can be used to distinguish the aforementioned models. The first is the location and morphology of diffusion region. In terms of location, the convective-diffusion (Section 2.2.1) and thin-film diffusion model (Section 2.2.2) have their diffusion layer outside the cavity. In contrast, the diffusion layer in the transient mass-transfer model (Section 2.2.3) exists inside the cavity. In general, the diffusion coefficient of a gas in water vapor is orders of magnitudes higher than in water, therefore, a more rapid equalization of the gas concentration inside the cavity is expected. In terms of morphology, the diffusion layer of the thin film model is a thin hollow-cylinder, that of the transient mass-transfer model is a cylindrical rod, and that of the convective-diffusion model is a self-similarly evolving gas-concentration profile. Clearly, the location motivates the assumption of accumulation in the diffusion layer, while the morphology of the diffusion layer motivates the concentration gradient of dissolved gases at the cavity's interface.

¹ In practice, a finite sequence of zero-crossings, α_n , suffices for calculating the concentration profiles. In this work, the first 50 zero-crossings of J_0 were considered, which corresponds to approximately 2% error relative to the converged value of the summation term.

The second distinguishing feature is the dependency of the diffusion-velocity, U_D , to the cavity radius, r_c . In the case of the transient mass-transfer model of Section 2.2.3, the diffusion velocity (see Eq. (20)) is inversely a function of the square of the cavity radius, and, also rapidly shrinks with increasing time. However, in both the thin-film model and the convective-diffusion model, the diffusion velocity is approximately constant, therefore independent of the cavity radius. Noting this similarity, it is instructive to understand the conditions at which both models would provide an equivalent prediction. We do this by equating the diffusion velocities of both models, therefore term U_D^{cd} of Eq. (11), and, the first-order approximation to U_D^{tf} from Eq. (16). We isolate an expression for the equivalent cavity length, \tilde{r}_c :

$$\tilde{r}_c \approx \frac{4U_\infty \delta_f^2}{\pi D} \quad (21)$$

The above expression can be further simplified by inserting a Reynolds number based on the cavity length, \tilde{r}_c instead of the film-thickness, δ_f , given by $Re_{\tilde{r}_c}$. In this case, we arrive at the expression:

$$\left(\frac{\tilde{r}_c}{\delta_f}\right)^2 \approx \frac{4}{\pi} Re_{\tilde{r}_c} Sc \quad (22)$$

Due to an assumption in the convective-diffusion approximation, that the Péclet number, $U_\infty \tilde{r}_c / D$, is always high, \tilde{r}_c it is at least much greater than the film-thickness, δ_f , needed to match the growth rate predictions with our observations.

2.2.5. Vortex-model choices

Besides the necessity of the vortex model to estimate the pressure-gradient at the cavity interface as indicated in Section 2.1, another purpose served by the vortex model is in the estimation internal concentration of air, c_{in} , as found in the cavity growth rate expressions Eqs. (11) and (15). (An internal concentration value is not needed for the mass-accumulator approach, Eq. (20), because the gas-concentration profile inside the cavity is estimated by the model.) Therefore, the most simplistic assumption for c_{in} in the external diffusion layer models is that of homogeneity, with the gas-concentration derived from its partial pressure through Henry's law. The partial gas-pressure can be estimated from the pressure balance (Eq. (4)) if the ambient pressure, vapor pressure, and a vortex-model accounting for the radial pressure gradient of the cavitating flow are available.

In this work, the analytical form of the cavitating Lamb–Oseen vortex model, as derived by Bosschers (2018a), was considered. He obtained jump-relations at the cavity interface for mass and momentum conservation equations (Bosschers et al., 2008) and obtained a vortex velocity profile given by Eq. (23). In this model, the radial distribution of the circumferential velocity (u_θ) of a infinite, cavitating vortex is given as:

$$u_\theta = \frac{\Gamma_\infty}{2\pi r} \left[1 - \beta e^{\left(-\zeta \frac{r^2}{r_v^2}\right)} \right]; r \in [0, \infty] \quad (23)$$

Here, r_v is the viscous core radius, Γ_∞ is the circulation strength and ζ is a constant equal to 1.2526. β accounts for the zero-shear stress boundary condition at the cavity interface. Eq. (23) the steady Lamb–Oseen vortex model when β equals 1. An expression for β is obtained by substituting Eq. (23) into the simplified momentum balance across the interface. This is given as:

$$\beta = \frac{r_v^2}{\zeta r_c^2 + r_v^2} e^{\zeta r_c^2 / r_v^2}. \quad (24)$$

For the assessment of our diffusion models against experimental data, we chose to use the vortex model of Bosschers et al. (2008). One concern in using this model is that the role of β as the cavity is developing is unknown. β typically has a small influence when $r_c / r_v \ll 1$ where its magnitude is close to 1. If β is left unbounded, it quickly grows in magnitude when the $r_c > r_v$. To circumvent this, we assume

that the viscous core will increase only to constrain the cavity size. If this is satisfied, the cavity interface will always be approximately at zero-shear stress condition during the growth-stage. This can be set into the vortex model as an *ad-hoc* correction where the β -parameter is set to a constant when $r_c = r_v$ during growth (see Bosschers (2018b)), thus, has a maximum value of 1.55. The implication of this assumption is that when the cavity size equals the viscous core size, further mass-transfer also expands the viscous core radius size equally.

It is also reasonable to assume that without a change in both the cavitation and Reynolds number, Γ_∞ is a constant. For comparison, we also consider the condition that $\beta = 1$ which reduces Eq. (23) to the steady Lamb–Oseen formulation. In this case, zero-shear stress across the boundary is disregarded and the cavity is assumed to be embedded within a static vortex. Finally, the pressure field around the cavity can be recovered by the simplified radial momentum balance:

$$\frac{\partial p}{\partial r} \approx \frac{\rho u_\theta^2}{r}, \quad (25)$$

which yields the following expression for the radial pressure distribution, as found in Bosschers (2018b), which we state here for convenience:

$$p_c(r_c) = p(r) - p_\infty = -\frac{\rho \Gamma_\infty^2}{(2\pi r)^2} \left\{ \frac{1}{2} - \beta \exp(-\zeta r^2 / r_v^2) + \frac{\beta^2}{2} \exp(-2\zeta r^2 / r_v^2) + \frac{\beta \zeta r^2}{r_v^2} \mathcal{E}_1\left(\frac{\zeta r^2}{r_v^2}\right) - \frac{\beta^2 \zeta r^2}{r_v^2} \mathcal{E}_1\left(\frac{2\zeta r^2}{r_v^2}\right) \right\}, \quad (26)$$

where \mathcal{E}_1 is the exponential integral function. In the following section, the experimental approach to measure the growth-rate of the cavity is described.

3. Experiments

In order to estimate the growth rate of the vortex cavity after inception and during its development, long-time shadowgraph measurements were performed at the cavitation flow loop at the Delft University of Technology. The experimental setup is described in Section 3.1, while, Section 3.2 describes the image processing and data reduction of the shadowgraph recordings for estimating the cavity size during its growth. As this water tunnel has a total water volume of only 6 cubic meters, the length of the flow loop is insufficient for dissolving all microbubbles in a single passage of the water in the flow loop. Its water quality can only be modulated by controlling the dissolved-gas content within the liquid. Therefore, two experimental procedures were used to judge the effect of the unaccounted nuclei content in the flow. This, along with our measurement approach for dissolved air concentration, is described in Section 3.3. Finally, Section 3.4 describes our measurement matrix and provides estimates of the uncertainties in the described results.

3.1. Measurement setup

A schematic of the measurement setup is provided in Fig. 3. The vortex cavity was generated by a stationary NACA 66(2)-415 elliptical half-wing with a root chord, C , of 12.56 cm which was set at an angle of attack of 9° to the flow with the suction side facing downwards. The freestream velocity, U_∞ , was stabilized by controlling the rpm of the pump, in order to maintain a steady pressure drop across the contraction-section (as described in Pennings (2016)). The ambient pressure was measured, both at the contraction inlet and exit, using a piezo-electric absolute pressure sensor (Keller PAA 33X) calibrated against a liquid column. This was set up as a redundant measurement to the differential pressure-sensor (Validyne DP 15) in order to validate its calibration. The linear regime of the flow-control system was

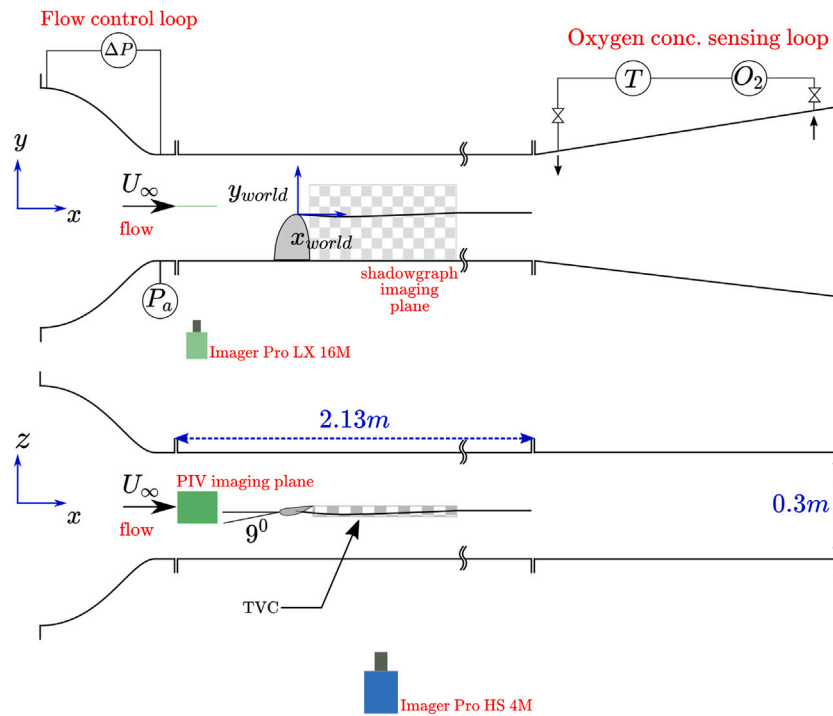


Fig. 3. A schematic description (not to scale) of the imaging and sensor setup in the cavitation tunnel (Pennings, 2016). Dimension lines are marked by dashed blue lines, while flow directions are black arrows. *Top*: Top-view of the setup showing the absolute and differential pressure sensors, respectively P_a and ΔP , attached to the contraction. The oxygen sensor and temperature sensor, respectively O_2 and T , are shown attached to the main diffuser on the right. *Bottom*: The side view of the same setup, showing the position of the camera and the inclination of the elliptical foil, suction side down. In both views, the calibration plane is shown using a schematic dot-pattern with the origin and orientation of the world-coordinate system indicated. The freestream velocity calibration plane is indicated in green. (For interpretation of the references to color in this figure legend, the reader is referred to the web version of this article.)

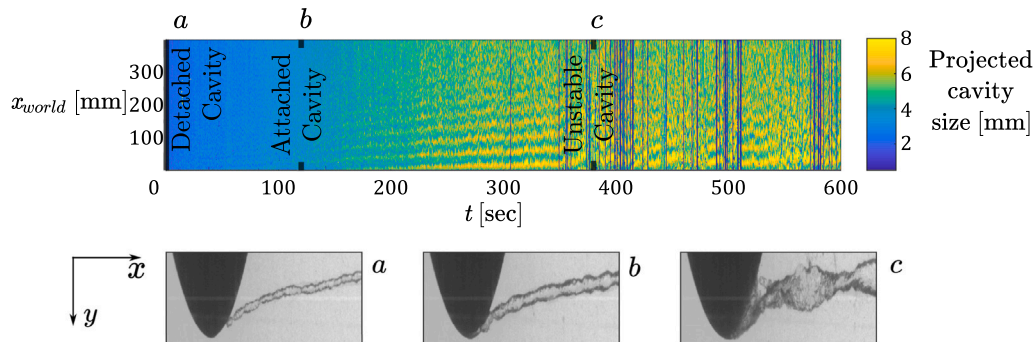


Fig. 4. Typical space-time curve of a wing-tip vortex cavity during its growth stage (in world-coordinate system). Measurement conditions are at $c_\infty/c_{sat} = 1$. The appearance of the cavity near the wingtip during its growth from detached, to attached, to finally at unstable conditions are marked in the space-time plot and shown below. The edge detection code in these circumstances fails and can be seen in the vertical bands of discontinuity in the space-time plot above.

ascertained using alternative planar Particle Image Velocimetry measurements of the flow entering the test section. Turbulence properties of the inflow were also inferred from the velocimetry recordings. The overall turbulence intensity was found to be below 1% of the mean velocity of 5.77 m/s.

In a typical measurement run, under-pressure conditions were first introduced to the tunnel at standstill conditions, following which, the flowrate was increased in stepwise manner until the intended cavitation number was reached, after which, the velocity was maintained. During the ramp-up of the flowrate, the cavitation initiates, and on completion of the ramp-up, the shadowgraph recordings are initiated. The shadowgraph recordings were continued while the cavity grows in size and is terminated when the cavity starts to cyclically collapse, rebound, and grow again. A typical space-time plot of the cavity size is shown in Fig. 4, which shows that the cavity is initially featureless, i.e., the cavity size is uniform along its axis, and visibly detached from

the tip. During growth, the cavity develops stationary waves on the surface, and after some development, attaches to the tip of the foil. Subsequently, the amplitude of the stationary wave increases, and the cavity becomes unstable, collapses and rebounds cyclically. This signals the termination of the cavity growth stage.

One important consequence of this experimental procedure is that the inception occurs during the ramp-up process, and that the vortex cavity has already slightly developed when the ramp-up is complete and the shadowgraph recordings commence. Therefore, the air concentration inside the cavity is expected to be non-zero from the start of the shadowgraph recordings. For this reason, we have chosen to compare our experimental data to predictions using a standardized Fourier number, which we discuss in Section 3.3. Our standardized Fourier number comparison is provided in Section 4.3.

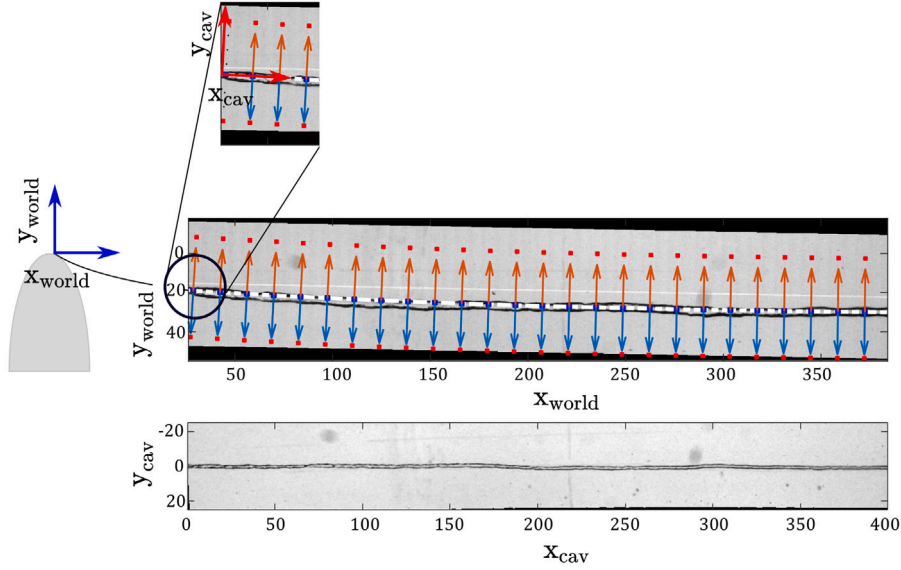


Fig. 5. Image transformation of the shadowgraph recordings. In this figure the flow is from left to right. *Top*: Cavity images in world-coordinate system. Cavity axis is given by dotted white lines, arrows indicate the cavity normal direction and red squares indicate the extents of the domain used for subsequent warping step. *Bottom*: Cavity shadowgraph presented in straightened format in averaged cavity-centerline coordinate system. All dimensions are provided in millimeters.

3.2. Imaging and image processing

The field of view was adjusted to cover the region from the wingtip and up to a maximum distance of 4.3 root-chord lengths downstream. The camera was calibrated using a laser-engraved 2D dot-target pattern of 1 cm dot-pitch placed at the vertical mid-plane of the test section, as shown in Fig. 3. A two-dimensional, third order polynomial mapping function similar to Soloff et al. (1997) was used for pixel-to-world coordinate transformation. This mapping function corrects for refraction through the thick acrylic wall of the test section and fits to the centroids of the imaged dots to within 0.1 pixels.

The cavity was imaged using an ImagerPro HS 4M high-speed camera mounted with a 35 mm Nikon objective. The image resolution was set to 2130×300 pixels, and the frame-rate of the high-speed camera was adjusted to provide a maximum of 30 minutes of observation time. Backlighting of the cavity was provided by a LED light-panel set to pulse with the camera shutter and with a pulse-width between 50–80 μ s. As the LED duty cycle is well below reported typical time-scales of cavity oscillations (Pennings et al., 2014; Arndt et al., 1991), motion blur on the cavity interface is avoided. The edges of the cavity are easier to extract using a scheme based on the gradient of the images. In this study, the Canny edge detector (Canny, 1986) was found to be suitable for extracting the cavity edges.

Once the cavity edges were detected, the projected centerline of the cavity was calculated from the midpoint between the upper and lower edges of the cavity. An ensemble averaged cavity centerline was then estimated from an ensemble of our recordings, which is shown in Fig. 5 in the world coordinate system. In order to dewarp the image so that the mean cavity centerline is the abscissa of the new coordinate system, its arc-length parametrization was first calculated using the following integral approach:

$$l_{cav} = \int_p^q \sqrt{1 + \left(\frac{dy}{dx}\right)^2} dx, \quad (27)$$

where, l_{cav} is the length of the cavity in the cavity centerline coordinate system between any 2 points p and q on x_{world} , and, y is position of the mean cavity centerline as a function of x_{world} .

To simplify this operation, the estimated position of the mean cavity centerline in y_{world} was replaced by a one-dimensional, second-order polynomial as a function of x_{world} with the resulting R^2 of the polynomial fit being 0.99. The polynomial was then reparametrized by

its arc-length using Eq. (27). The resulting new coordinate system has the abscissa as the arc-length parametrized form of the mean-cavity axis (x_{cav}) and the ordinate as the direction normal to the tangent of the mean cavity axis in world coordinate system (y_{cav}). This finally helps generate a cartesian grid in the new coordinate system, which appears warped in the world coordinate system, as indicated in Fig. 5. Finally, a two-dimensional, homogeneous polynomial is used to warp the image from world-coordinate system to the cavity axis system (see Fig. 5). Here, the fitting error, defined as the euclidean distance between the axis system of the unstraightened cavity images and the new grid in the cavity axis centered coordinate system (as described in Fig. 5), was found to be less than 10^{-3} mm and therefore not considered in the error analysis. The final resolution of the image in cavity-axis system is 0.18 mm in cavity-axis direction and 0.125 mm in cavity-transverse direction.

In the last step of the image processing, the cavity's projected diameter was estimated from the dewarped cavity edges in the new coordinate system. The resulting cavity growth curves were averaged along the axis-direction for each time-step, following which, a running time-average filter over 500 timesteps was applied to the cavity size time-history.

3.3. Dissolved gas monitoring

In the present experiments, the ambient dissolved gas level was varied between 28% to 41% air-saturation relative to atmospheric conditions. Under the assumption that the partial fraction of gases in air remains unchanged in underpressure conditions, the dissolved oxygen content was measured as a proxy to the air content. This was monitored by an on-line, optical, dissolved oxygen probe of the flow-through type (PreSens FTM type) whose working principle is based on the fluorescence-quenching mechanism of oxygen molecules. The sensor was housed in a parallel pipe-branching connected to the points near the inlet and exit of the main-diffuser as shown in Fig. 3. In such a configuration, the natural pressure-drop of the diffuser drives a flow inside the branching which refreshes the sampled tunnel water dynamically, giving reliable results during running conditions. The tunnel has a relatively low water volume of about 6 cubic meters, therefore, at the measurement conditions, the typical flow through time between the hydrofoil and the measurement probe is of $\mathcal{O}(1)$ seconds. In standstill conditions, the ambient pressure on the foil region is also

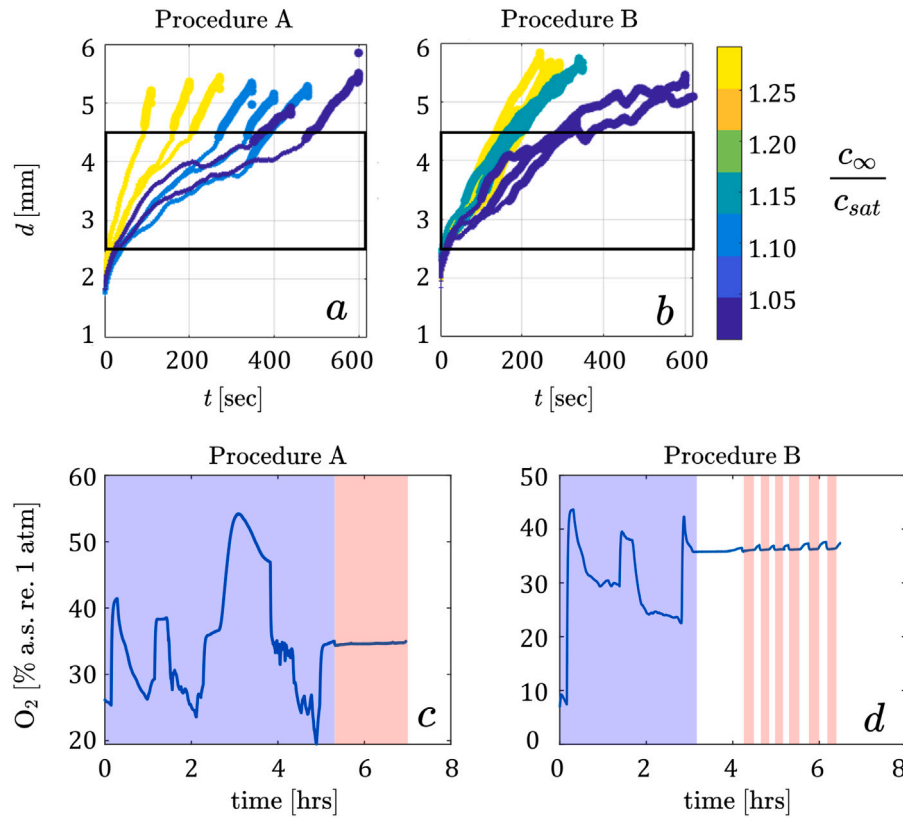


Fig. 6. **a and b:** Time-history of the filtered and axially averaged cavity diameter $d := 2r_c$, over the observation period, t , for both measurement procedures described in Section 3.3 and tabulated in Table 2. The time-histories are colored with respect to the relative saturation level, c_∞/c_{sat} , and the marker thickness is increased when the cavity appears to attach to the wing-tip. The growth period between growth ranges of 2.5 mm and 4.5 mm is highlighted by the boundaries of the black boxes superimposed on the text. **c and d:** Oxygen-content measured by the dissolved-oxygen probe represented as a percentage air-saturation relative to 1 atm and operating temperatures. The degassing phase is highlighted in blue whereas red highlights the time-history when the measurement run commenced, and the tunnel is running either at idling (3 m/s) or testing conditions. In the figure on the right, shark-fin like deviations is seen in between the measurement runs when the tunnel is stopped and vacuum is removed. In the blank regions, the tunnel is in a shut down state without underpressure or a flow. (For interpretation of the references to color in this figure legend, the reader is referred to the web version of this article.)

similar to the probe location. Therefore, the sampled water can be thought to be a reliable proxy to the measured dissolved gas in the test section. A PT100 type temperature sensor, compatible with the oxygen sensor's data acquisition system, was also installed to account for temperature changes to the measured oxygen content level. In this work, the oxygen concentration is quoted as % air saturation relative to atmospheric pressure and measured temperature. Repeat observations were performed on the same day, and, three dissolved-gas levels were chosen, with each gas-level set on a different day. The dissolved-gas content was reduced every subsequent measurement day and repeat measurements were performed on the same day. The measurement procedure was also varied, in the first procedure (procedure A), the facility is not shut down between the repeat runs, while in the second procedure (procedure B), the facility is shut down between the repeat runs in order to remove microbubbles from the flow.

Because of the flow-through nature of the sensor, the dissolved air-content measurement is sensitive to the presence of a flow in the accompanying diffuser. On stopping the flow, the oxygen sensor reported increasing gas-content due to microbubbles dissolving locally near the probe, thus, de-correlating the sample population present in the sensor branch from the parent population. This is characterized by the shark-fin like deviations on the oxygen sensor recording and is shown in the right panel of Fig. 6 (procedure B), which are not found when a flow in the tunnel is always present (left panel of Fig. 6, procedure A). Noting that both procedures significantly differ in terms of how much nuclei content is available in the tunnel prior to a measurement, it is important to distinguish between both measurement procedures as shown in Fig. 6 into one where tunnel's free-gas content is unaltered (procedure A) during the course of the day while the second procedure is where

the tunnel's free-gas content is reset by reintroducing atmosphere and stopping the flow between runs (procedure B). The top panels of Fig. 6 also show the time-history of the measured cavity-radius.

A few observations from Fig. 6 are clear. Firstly, in both measurement procedures, an increase in the relative saturation content of air in ambient flow-conditions increases the growth rate of the cavitation. Secondly, measurement repeatability is severely affected by the increasing nuclei-number-density of bubbles when using measurement procedure A. Finally, the most puzzling aspect is that the attachment of cavity during its growth is delayed in measurements using procedure A. The cause for this observation is unclear and has not been pursued in this work. From these observations, the measurements using procedure B were chosen for further analysis. As the effect of unaccounted free-gas bubbles are presumably lesser. More importantly, the repeatability of the experiment is enhanced. Therefore, the measurements can be said to be in nuclei depleted conditions.

3.4. Measurement matrix and measurement spread

In the present work, the chord Reynolds number (Re_c) and cavitation number (σ) are defined as:

$$Re_c = \frac{U_\infty C}{\nu} \quad (28)$$

$$\sigma = \frac{p_\infty - p_{vap}}{0.5 \rho_l U_\infty^2} \quad (29)$$

The measurement matrix of the observations found in this work is provided in Table 2. In this tabulation, we also provide the F_m estimated over a fixed growth range of the cavity diameter, i.e., from

Table 2

Measurement data for both measurement procedures including the inflow cavitation number, σ , the dissolved gas content expressed relative to saturation conditions at the set test section pressure, c_∞/c_{sat} , and estimates of \bar{F}_m numbers from experimental measurements for the time duration (Δt), extrapolated from data, for a change in cavity projected diameter from 2.5 mm to 4.5 mm, as highlighted by gray in Fig. 6. One measurement in set 6 was terminated prematurely but has been included in the table and highlighted with an asterisk. In all the calculations the freestream velocity is taken as 5.77 m/s.

Procedure	p_∞	T	Re_c	σ	O_2	c_∞/c_{sat}	Δt	\bar{F}_m
[–]	[mbar]	[°C]	[$\times 10^5$]	[–]	[% <i>re.1atm</i>]	[–]	[s]	[–]
1 A	250	20.7	7.35	1.3	41.00	1.51	145.55	0.29
			7.35				189.93	0.37
			7.30				83.56	0.16
2 A	300	21.0	7.35	1.4	37.00	1.36	309.32	0.61
			7.40				354.12	0.70
			7.40				233.80	0.46
3 A	300	21.3	7.45	1.4	34.50	1.27	349.10	0.69
			7.45				455.04	0.91
4 B	275	21.6	7.50	1.2	36.30	1.33	183.32	0.36
			7.50				136.62	0.27
			7.50				126.90	0.25
5 B	275	21.5	7.50	1.2	32.40	1.19	182.49	0.36
			7.50				190.40	0.38
			7.50				162.77	0.32
6 B	275	22.0	7.60	1.2	28.15	1.04	275.07	0.55
			7.60				280.05*	0.56
			7.60				358.79	0.71

2.5 mm to 4.5 mm. The time elapsed between these two bounds is also provided in the table. The relative saturation of air in water, c_∞/c_{sat} , is provided with c_{sat} determined at the working ambient pressure, p_∞ , using Henry's law. We refer to this form of standardization of F_m as \bar{F}_m . It will be clear in Section 4.3 that this standardization helps enable the comparison of our experimental data with our predictions.

The estimation of the spread in the reported experimental parameters was performed using the Monte-Carlo error propagation procedure described by Coleman and Steele (2018), with the input quantities assumed to be normally distributed. The error propagation begins with the voltage output of the pressure sensor, whose typical standard deviation of about 2% of the mean measured voltage, while the temperature sensor has a typical standard deviation of about 1% of the mean measured. The standard deviation of the voltage of the temperature and pressure sensor were used to estimate the histogram of the measured temperature, pressure, and freestream velocities from their respective calibration functions. The obtained distributions were then used to estimate the same for the density, dynamic viscosity and vapor pressure of water using standard temperature correlations. Finally, the probability distributions of density, dynamic viscosity and vapor pressure were used to estimate the same for the chord Reynolds number of the flow, and the cavitation number of the measurement. For the relative air-saturation concentration, the spread of the dissolved oxygen sensor was ignored as its magnitude is very small. Therefore, the spread in this quantity is largely due to that present in the ambient pressure measurement. The edge detection performed for the images is deterministic, hence, the spread in the measured cavity size is of the order of the pixel resolution in cavity centerline coordinate system, y_{cav} , therefore 0.125 mm. The spread of the smoothed cavity size time-history is based on the standard deviation of the running average performed over 500 timesteps and presented as shaded uncertainty envelopes in the figures following this section. In the following discussion, we report the measurement spread as the 95% confidence bound of the estimated probability distributions of the quantities reported.

From the Monte-Carlo error propagation approach, the estimated chord Reynolds number, Re_c , varied between 7.3×10^5 and 7.5×10^5 with an spread of 1.25%, 4.08% spread in the cavitation number, which was achieved with an input measured inflow velocity distribution of

5.77 m/s with 1.05% uncertainty. The spread of the measured ambient pressure, therefore, that of the relative saturation level at ambient pressure conditions of the measurement, was 3.18%.

4. Results and discussions

In Sections 4.1 and 4.2, we first present and discuss the cavity radius predictions of Eqs. (11), (15) and (20) for typical experimental values of the vortex viscous core, the incipient cavity radius and the relative saturation of the ambient dissolved gas content. For convenience, we divide this discussion into two parts: In Section 4.1 we discuss the predicted growth behavior for relatively saturated and oversaturated dissolved gas conditions; and, in Section 4.2, we show the same for undersaturated conditions, where stable cavity sizes can be sought. Then, in Section 4.3 we compare the predictions of the diffusion models with experimental data using a Monte-Carlo approach.

Solving the equations of the cavity growth rate (Section 2) requires a careful consideration of the parametric entries. The parametric entries are divided into three parts. The first set concerns known thermodynamic and kinematic properties of water and the gases dissolved in it (Table 3), which we take to be air. This contains the molecular weight of air (M_g), density of air and water (ρ_g and ρ_l , respectively), Henry's constant for air dissolved in water (K_H), the water temperature (T), the binary diffusion coefficient for air in water (D), and the surface tension coefficient of pure-water (\mathcal{T}). With regards to the binary diffusion coefficient, we assume a magnitude of 2×10^{-9} m²/s for the external diffusion models described in Sections 2.2.1 and 2.2.2. For the internal diffusion model, we assume the diffusion coefficient, \bar{D} , to be that of air in water-vapor. We assume this to be a magnitude 10^3 times higher than D , which is approximately the diffusion coefficient of oxygen in water-vapor (2.4×10^{-5} m²/s at 20 °C). We also include the tunnel ambient pressure, p_∞ , and the ambient dissolved gas concentration, c_∞ , in this categorization.

The second set of parameters (Table 4) are the flow dependent properties of the vortex cavitation. They consist of the incipient vortex cavity size, r_c^i , the size of the vortex viscous-core, r_v , the β parameter which varies the vortex model between the steady Lamb–Oseen vortex model ($\beta = 1$), or, the *ad-hoc* correction described in Section 2.2.5. The ambient circulation strength (Γ_∞), is back-calculated from the vortex model using the assumed viscous-core size, the expression for the pressure distribution of the vortex (Eq. (26)), and, the pressure balance of Eq. (4) at inception conditions, i.e., when p_{in}^g is zero.

The third set of parameters (Table 5) relate to the diffusion velocities of the individual diffusion models. They are the cavity length for the convective-diffusion model, either l_c , or, \bar{l}_c , and, the film-thickness, δ_f , for the thin-film diffusion model. Both these quantities are treated as tuning parameters to match the predictions with our experimental data. We note here that the diffusion velocity of the transient mass transfer model of Section 2.2.3 is dependent on the diffusion coefficient and the cavity radius alone. We also include in the table the equivalent cavity length parameter (Eq. (21)) for the convective-diffusion model (Section 2.2.1).

The growth rate equations are solved using a first-order time-stepping approach. The simulations are set to begin at inception conditions, and, in these conditions, the internal air-concentration in the cavity is assumed to be zero. Therefore, the growth of the cavity always begins with the cavity being saturated with water vapor at its vapor pressure, p_{vap} . After each incremental timestep in which a new cavity radius is estimated, the pressure of air and its concentration inside the cavity ($p_{in}^g(t)$ and c_{in} , respectively) are evaluated from the pressure balance of Eq. (4) and Henry's law, respectively. In order to do so, the pressure at the cavity's interface, $p_c(r_c)$, is estimated from the vortex-model, Eq. (26). The effect of surface tension is captured in $p_T(r_c)$, and is given by the expression \mathcal{T}/r_c .

Table 3

A tabulation of the material properties used for the analyses in Sections 4.1 and 4.3. Asterisk superscript indicates range of values.

	Symbol	Units	Sections 4.1, 4.2	Section 4.3.1	Section 4.3.2
Molecular weight of air	M_g	kg/mol		28.96×10^{-3}	
Water temperature	T	K	295	Table 2	295
Universal gas constant	R	J/mol K		8.314	
Air and water density	ρ^g, ρ_l	kg/m ³		$M_g/RT, 10^3$	
Henry's constant	K_H	kg/m ³ Pa		0.223×10^{-6}	
Diffusion coefficient (air–water)	D	m ² /s		2×10^{-9}	
Diffusion coefficient (air–water vapor)	\tilde{D}	m ² /s		2×10^{-5}	
Ambient pressure	p_∞	Pa	30 000	Table 2	Table 1
Ambient dissolved gas concentration	c_∞	kg/m ³	(0.1 to 2) $K_H p_\infty^*$	Table 2	Table 1
Vapor pressure of water	p_{vap}	Pa		Clausius–Clapeyron	
Surface tension	\mathcal{T}	N/m		0.071	

Table 4

A tabulation of the flow related properties used for the analyses in Sections 4.1 and 4.3. The expression for vortex-viscous core size is based on a Winckelman-vortex model (Gerz et al., 2005) fit to the stereoscopic PIV measurements found in Pennings (2016). The root-chord length of the foils considered in the analyses (C) are 12.56 cm in Section 4.3.1 and 47.5 cm in Section 4.3.2. Quantities with asterisk superscript are estimated at the first timestep. Γ_∞ for Section 4.3 is given as the average of the set of predictions. A double asterisk indicates that the magnitude is corrected to match experimental data.

	Symbol	Units	Sections 4.1, 4.2	Section 4.3.1	Section 4.3.2
Incipient cavity radius	r_c^i	mm	0.5	$0.125 \leq r_c^i \leq 0.2$	1, 1.5
Viscous-core radius	r_v	mm	2.5	Eq. (31)	2, 4.5**
Ambient circulation strength	Γ_∞	m ² /s	0.09*	0.04*	0.2, 0.45**

Table 5

A tabulation of the diffusion model parameters used for tuning in Sections 4.1 and 4.3.

	Symbol	Units	Sections 4.1, 4.2	Sections 4.3.1, 4.3.2
Cavity length for U_D^{cd}	l_c	m	1.7	–
Equivalent cavity length for U_D^{cd}	\tilde{l}_c	m	0.36	0.18
Film thickness for U_D^f	δ_f	μm	10	5

4.1. Behavior of the diffusion models in saturated and oversaturated dissolved gas conditions

Fig. 7 describes the magnitude of the cavity diameter predicted by the diffusion models of Section 2 using the input values described in Tables 3–5. The first discussion concerns the condition when c_∞/c_{sat} is 1.35, where the growth of the cavity radius over time, and the increasing pressure of air inside the cavity during its growth, are plotted for all three diffusion models in the top two figures. Firstly, the transient mass-transfer model (Section 2.2.3) predicts a rapid stabilization of the cavity radius to about 650 μm from its incipient cavity radius of 500 μm in a time-duration of 0.2 s, which gives a Fourier number ($F_m = \Delta t \tilde{D}/\Delta r_c^2$) of 17.7 highlighting that the diffusion has sufficiently advanced in only 0.2 s. This behavior indicates that the concentration is quickly equalized when the cavity size is small and agrees with our heat-conduction analogy indicated in Section 2.2.3, where the temperature in a thin wire suddenly exposed to heat equalizes much faster than that in thicker rods. This predicted behavior is clearly not what is observed in experiments (see Fig. 6) and invalidates the model for the purpose of predicting the cavity radius. Therefore, the transient mass-transfer model is not considered any further. The rapid equalization feature of this model, however, does help motivate the homogeneity of the gas-concentration inside the cavity, which is a central assumption in the convective-diffusion model and the thin-film model.

From the same figure, we also observe that both the convective-diffusion and the thin-film models predict reasonably similar cavity growth rates and internal gas-concentration behavior. This is expected given that these models yield identical results for a specific choice of the cavity length or the diffusion layer thickness. We also observe that the *ad-hoc* modification to the Lamb–Oseen vortex model has a marginal impact on the prediction of the cavity size. Therefore, we can conclude that the choice of the vortex model has limited advantage in the prediction of the cavity growth behavior. This can also be inferred from the standardized Fourier number (\tilde{F}_m) comparison in Fig. 7.c. Overall, it is clear that the relative saturation rate c_∞/c_{sat} , and the

diffusion velocity parameters have the largest influence on the growth behavior estimated by the diffusion models of Eqs. (11) and (15). This can be inferred from the predicted \tilde{F}_m behavior for the thin-film model at $t_f = 9 \mu\text{m}$, which corresponds to an equivalent cavity length, $\tilde{l}_c = 0.36 \text{ m}$, for the convective-diffusion model (as indicated in Table 5). For the subsequent discussion, we make use only of the convective-diffusion and the thin-film diffusion model.

4.2. Behavior of the diffusion models in undersaturated dissolved gas conditions

If stable cavity sizes are intended, the relative saturation level must necessarily be lower than 1. In this regard, it is important to understand how long the diffusion process needs to advance for stability to be achieved at a given undersaturated flow-condition. To study this, we conduct simulations with $c_\infty/c_{sat} < 1$ and estimate a new Fourier number, $F'_m = t' D/r_{in}^2$, where t' is the time elapsed following inception when the change in cavity radius is less than $10^{-3} \mu\text{m}$.

Fig. 8, left, provides the behavior of the convective-diffusion model and the thin-film model for a series of undersaturated dissolved gas conditions. The main observation is that stable cavity sizes are possible when $c_\infty/c_{sat} < 1$, however, the final size of the vortex cavity strongly depends on the degree of undersaturation. Furthermore, the estimated F'_m suggests that the diffusion needs to advance for long diffusion timescales the closer c_∞/c_{sat} is to 1. Note that in this assessment, we ignore the upper bounds to the cavity size which we have observed in our experiments (see Fig. 4).

Both the convective-diffusion model with $l_c = 1.7 \text{ m}$, and the thin-film model with $t_f = 10 \mu\text{m}$ predict the same final cavity size despite having different growth-rates. This suggest that the final stable cavity size is independent of the diffusion model choice. It is possible to estimate the stable cavity radius in undersaturated conditions in the following manner. At equilibrium, c_{in} equals c_∞ . Therefore, from Henry's law, the gas pressure inside the cavity is then equal to $c_\infty p_\infty/c_{sat}$. This

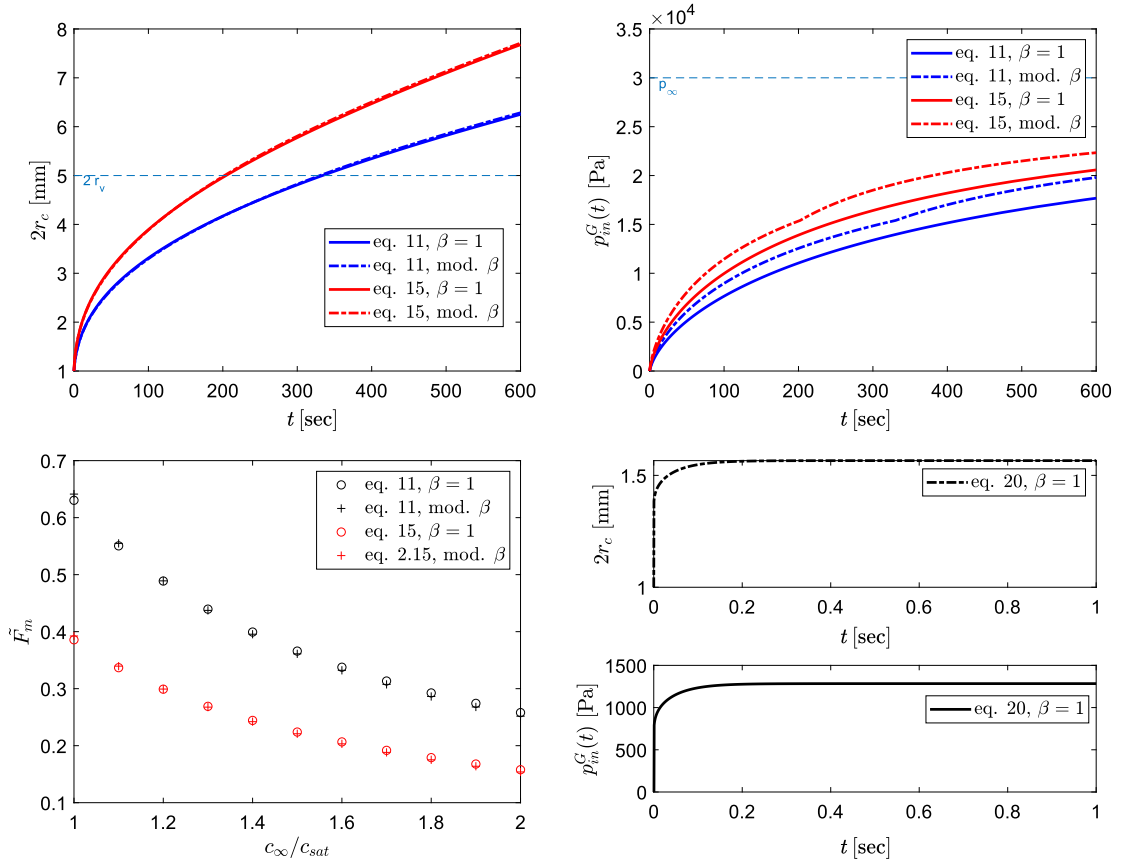


Fig. 7. Behavior of the diffusion models (Section 2) for the parameters described in Tables 3–5. The vortex model chosen for the simulations are given by their respective β -parameter behavior in the legend, as described in Section 2.2.5. For figures a & b, the relative saturation level at p_∞ (c_∞/c_{sat}) is 1.35 (or 40% air-saturation re. 1 atm), while, for figure c, this is varied from 1 (saturated) to 2 (oversaturated). a: Evolution of cavity diameter over time. The transient mass-transfer model (Eq. (20)) is indicated in a sub-figure. For convenience, $2r_{vs}$ is indicated where the modification to the Lamb–Oseen model is activated when $\beta \neq 1$. b: The evolving pressure of gas (air) inside the cavity for the simulations of sub-figure a. c: The estimation of \bar{F}_m (defined in Table 2) for c_∞/c_{sat} varied between 1 and 2. d: The cavity diameter evolution for the transient mass-transfer model. Top figure of d corresponds to the radius evolution over time, while the bottom figure of d corresponds to the gas pressure inside the cavity over time.

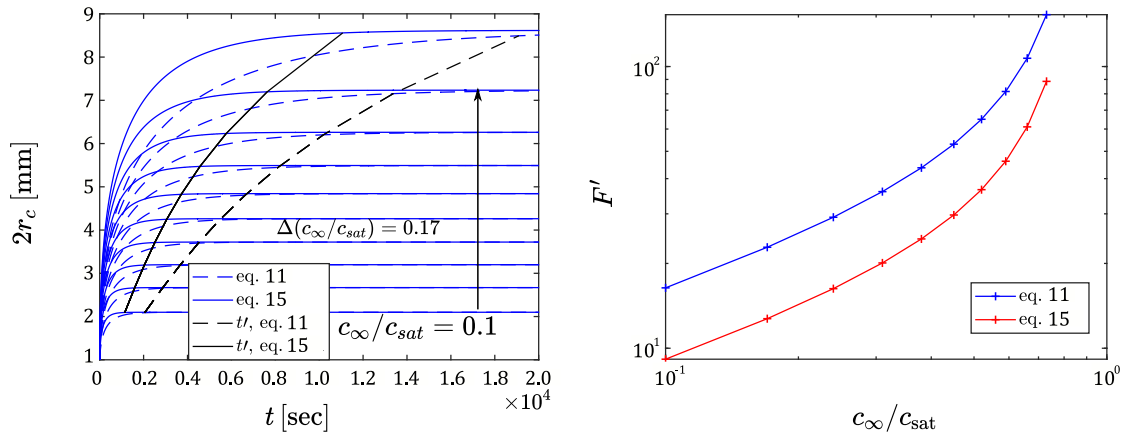


Fig. 8. Behavior of the diffusion models in undersaturated conditions for parameters of Tables 3–5. Left: Cavity radius predictions by the diffusion models in undersaturated dissolved gas conditions, where c_∞/c_{sat} is varied from 0.1 onward with a step size of 0.17. The terminal time of the growth, t' , is indicated by black lines. Right: Estimation of F' for the simulations conducted in the left figure for both diffusion models. For the analyses, the Lamb–Oseen vortex model is used ($\beta = 1$).

can be substituted to Eq. (4) which results in the following expression for the cavity interface pressure in stable cavity size conditions:

$$p_c = p_\infty(c_\infty/c_{sat} - 1) + p_{vap} - p_T. \quad (30)$$

The above expression can be substituted into the pressure equation of a vortex model, such as that in Eq. (26), and through a least-squares

approach, the stable cavity radius required to balance both sides of the expression can be estimated. This demonstrates that an estimate of the stable cavity size is largely defined by the radial pressure profile of the vortex-cavity, which in turn depends on the vortex-model considered. As velocimetry around the vortex-cavity was outside the scope of this work, this analysis has not been considered any further.

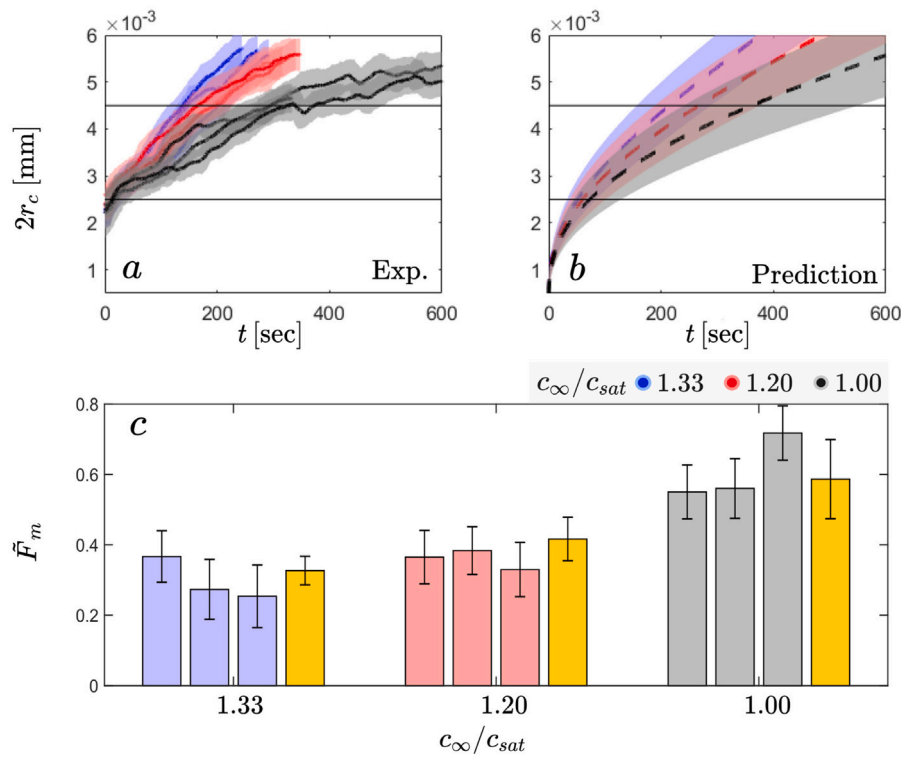


Fig. 9. Comparison of the experimental observations in the oversaturated regime with the diffusion model predictions for chosen parametric entries (Tables 3–5). *Top:* Comparison of the growth of the vortex cavity size, $2r_c$, with the experimental data, procedure B, from Table 2. The uncertainty envelopes correspond to two standard deviation bounds. Horizontal lines correspond to the size range used to evaluate the standardized Fourier number, \tilde{F}_m . *Bottom:* Bar chart comparing Experimental \tilde{F}_m values obtained from repeated measurements, color coded according to their respective c_∞/c_{sat} values, while yellow bars are their corresponding predictions. The error bars here represent the one standard deviation bound of the output probability distribution of \tilde{F}_m .

4.3. Comparison with experimental data

In this discussion, we use the thin-film model as the base diffusion model for our analyses and represent the convective-diffusion model by its equivalent length parameter, \tilde{l}_c . As noted from our previous discussion in Section 4.1, the vortex model we have chosen for this analysis is the steady Lamb–Oseen vortex model.

4.3.1. Oversaturated regime

As remarked earlier in Section 3.1, the incipient vortex cavity size in our observations is unknown. This is important to note because the incipient cavity size is an important vortex cavity parameter in our models (see Tables 3–5). Therefore, we introduced the standardized Fourier number, \tilde{F}_m , in Section 3.3, which compares the growth rate within a fixed cavity growth range. Further, the vortex viscous-core size is unknown in the present experiments, therefore, we take a Monte-Carlo simulation approach to estimate the prediction spread for both r_c , as well as, \tilde{F}_m . In this procedure, both the vortex cavity parameters, r_c^i and r_v , are varied within a reasonable range. For the viscous-core radius estimate, we refer to the work of Pennings et al. (2015) where a Winkelman vortex model fit to their experimental data is given by the following expression:

$$r_v = B \cdot 0.37CRe_c^{-0.2}/10^3, \quad (31)$$

where B varies between 0.3 and 0.5, depending on the distance from the tip. For the incipient cavity radius, we choose a range between 125 μm and 200 μm , which is in range of the typical nuclei radius expected in the tunnel.

Fig. 9 details the comparison of our experimental data with the diffusion model predictions. In the comparison, the resulting probability distributions of \tilde{F}_m predictions were found to be non-normal, therefore, the predicted \tilde{F}_m is expressed as a mean value and the error

bars are defined by one standard deviation of the distribution. From the figure, we find that the diffusion models offer a reasonable prediction of the cavity growth rate for an assumed film-thickness, δ_f , of 5 μm , or, an equivalent cavity length, \tilde{l}_c , of 0.18 m. It is concluded that the growth-behavior of a cavitating vortex is largely driven by molecular diffusion in nuclei depleted conditions. However, this comparison does not distinguish between the thin-film model and the convective-diffusion model, leaving the detailed mechanism of vortex-cavitation growth speculative. With the convective-diffusion approach, it is clear that the length of the cavity needed for the comparison is not what is observed in experiments where the cavity length is observably at least as long as the length of the test-section following the hydrofoil tip. For applying this model to experimental data, an estimate of the possible equivalent cavity length remains unknown. What is striking is that, the estimated magnitude of \tilde{l}_c , 0.18 m, is quite close to the root-chord length of the wing-tip used. The scope of our analyses presented here do not suffice to explain this occurrence, therefore, this observation remains coincidental. Similarly for the thin-film diffusion model, while a film thickness of 5 μm suffices to explain the observed growth rate, and, even though the criteria that $r_c \gg \delta_f$ is satisfied, the physical mechanisms that eventually lead to the formation of this thin-layer is unknown. Therefore, the choice between these two modeling approaches remains open.

4.3.2. Undersaturated regime

Comparison against experimental data for the undersaturated regime was made possible from the cavity diameter time-histories reported by Briançon-Marjollet and Merle (1996).² The experimental

² These conditions were not possible in the facility used for the present study because the tunnel's ambient pressure could not be increased beyond 1 atm to lower c_∞/c_{sat} below 1.

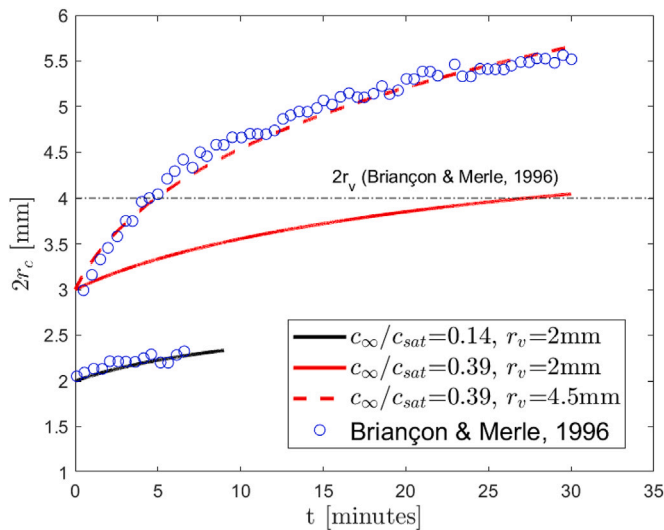


Fig. 10. Comparison of the experimental observations of Briançon-Marjollet and Merle (1996) in the undersaturated regime with diffusion model predictions for chosen parametric entries (Tables 3–5).

conditions concerned here are the *small-nuclei* cases considered for c_∞/c_{sat} , p_∞ , U_∞ and σ found in rows 1 and 2 of Table 1, whose relevant properties have been summarized in Tables 3–5. For the model predictions, we have assumed that the cavity size data provided at the first timestep corresponded to inception conditions. The comparison against experimental data is provided in Fig. 10. For the case where the relative undersaturation is 0.14, a reasonable comparison between both the predicted and observed cavity diameter time-histories was observed. The performance of the diffusion model could not be replicated for relative undersaturation of 0.39 using the experimental conditions as provided in Briançon-Marjollet and Merle (1996). In order to match the data, a modification to the viscous core radius to 4.5 mm had to be made. As stated previously, the chosen vortex model (here, the static Lamb–Oseen model) also plays a role in the prediction of the time-history, therefore, an exact match of the predictions in the temporal space is difficult.

While a quantitative comparison using the above results is difficult, the predictions qualitatively agree with the experimental data, thus supporting the discussion in Section 4.2. This means that in the undersaturated regime, the size of the stable cavity is proportional to the degree of undersaturation.

5. Conclusions

In nuclei depleted conditions, the mechanism of vortex cavity growth following inception can be described as a diffusion dominant phenomenon. Gases dissolved in the liquid enter the vortex cavity through a diffusion layer whose morphology is either hollow-cylinder like (thin-film model), or, developing boundary layer like (convective-diffusion model). From the assumptions common to both the thin-film and the convective-diffusion model, the concentration of air inside the cavity can be thought to be homogeneous. It was found that the convective-diffusion model predicts the growth rate of the cavity reasonably well but requires a cavity length parameter that does not correspond to the physical length of the observed cavitation. In contrast, the thickness of the diffusion layer in the thin film does satisfy the condition $\delta_f \ll r_c$, making it a more appealing description of the diffusion phenomenon. However, physical motivations of the thickness of this diffusion layer remain unknown. Furthermore, in oversaturated conditions we found that the details of the vortex model used in the pressure balance across the interface did not significantly change its growth behavior.

In saturated and oversaturated dissolved gas conditions, $c_\infty/c_{sat} \geq 1$, the diffusion process does not terminate. Consequently, the cavity grows uncontrollably until it becomes unstable, and its size seems to oscillate. The conditions for the upper bounds on the cavity size is not presently known. In undersaturated dissolved gas conditions, $c_\infty/c_{sat} < 1$, the details of the diffusion model were found to not affect the final stable size of the vortex cavity. Rather, we find that the vortex cavity size in undersaturated dissolved gas conditions depends on the pressure profile around the vortex cavity, and the degree of undersaturation. Further understanding of the role of the vortex velocity profile in the rate of growth of vortex cavities is necessary.

The growth behavior of the vortex cavity was found to be fairly repeatable in nuclei depleted conditions, and strongly affected by nuclei in weak-water conditions, although, the influence of the relative saturation of dissolved gases could still be discerned from the non-repeatable measurements. In cavitation tunnels that do not have provisions for water quality control, it is possible to obtain repeat experiments by shutting down the cavitation tunnel and introducing the tunnel to atmospheric pressure between runs. This provides the residence time for the gas bubbles to either separate due to their buoyancy, or reabsorb back into the solution. If stable cavity sizes are intended, the degree of undersaturation must be high so as to reduce the diffusion time-scales ($F' = 1$) required before the cavity size stabilizes.

CRedit authorship contribution statement

Swaraj Nanda: Conceptualization, Methodology, Software, Formal analysis, Investigation, Visualization, Validation, Formal analysis, Writing – original draft. **Jerry Westerweel:** Conceptualization, Methodology, Supervision, Writing – review & editing. **Tom van Terwisga:** Conceptualization, Supervision, Writing – review & editing, Funding acquisition. **Gerrit Elsinga:** Methodology, Supervision, Formal analysis, Writing – review & editing, Project administration, Funding acquisition.

Declaration of competing interest

The authors declare that they have no known competing financial interests or personal relationships that could have appeared to influence the work reported in this paper.

Acknowledgments

This research was financially supported by the Dutch Research Council (NWO), The Netherlands, as part of the NOISOURCE, The Netherlands project (ALWTW.2016.008), and by the Dutch Ministry of Economic Affairs, The Netherlands. The authors would like to thank Johan Bosschers of MARIN for his comments during the development of this work.

References

- Amini, A., Reclari, M., Sano, T., Iino, M., Dreyer, M., Farhat, M., 2019. On the physical mechanism of tip vortex cavitation hysteresis. *Exp. Fluids* 60 (7), 118.
- Arndt, Roger E.A., 2002. Cavitation in vortical flows. *Annu. Rev. Fluid Mech.* 34 (1), 143–175.
- Arndt, R.E.A., Arakeri, V.H., Higuchi, H., 1991. Some observations of tip-vortex cavitation. *J. Fluid Mech.* 229, 269–289.
- Arndt, R.E.A., Keller, A.P., 1992. Water quality effects on cavitation inception in a trailing vortex. *J. Fluids Eng.* 114 (3), 430–438.
- Arndt, R.E.A., Maines, B.H., 2000. Nucleation and bubble dynamics in vortical flows. *J. Fluids Eng.* 122 (3), 488–493.
- Atlar, M., 2002. The specialist committee on water quality and cavitation—final report. In: *Proceedings of the 23rd ITTC*, Vol. 2.
- Billet, M.L., Weir, D.S., 1975. The effect of gas diffusion on the flow coefficient for a ventilated cavity. *J. Fluids Eng.* 97 (4), 501–505.
- Bosschers, J., 2018a. An analytical and semi-empirical model for the viscous flow around a vortex cavity. *Int. J. Multiph. Flow.* 105, 122–133.
- Bosschers, J., 2018b. *Propeller Tip-Vortex Cavitation and Its Broadband Noise* (Ph.D. thesis). University of Twente.

- Bosschers, J., Janssen, A.A., Hoeijmakers, H.W.M., 2008. Similarity solutions for viscous cavitating vortex cores. *J. Hydrodyn. Ser. B* 20 (6), 679–688.
- Brennen, C., 1969. The dynamic balances of dissolved air and heat in natural cavity flows. *J. Fluid Mech.* 37 (1), 115–127.
- Brennen, C.E., 2014. *Cavitation and Bubble Dynamics*. Cambridge University Press.
- Briançon-Marjollet, L., Merle, L., 1996. Inception, development and noise of a tip vortex cavitation. In: 21st Symp. on Naval Hydrodynamics, Trondheim, Norway.
- Canny, J., 1986. A computational approach to edge detection. *IEEE Trans. Pattern Anal. Mach. Intell.* (6), 679–698.
- Chen, Linya, Zhang, Lingxin, Peng, Xiaoxing, Shao, Xueming, 2019. Influence of water quality on the tip vortex cavitation inception. *Phys. Fluids* 31 (2), 023303.
- Cheng, Huai-yu, Ji, Bin, Long, Xin-ping, Huai, Wen-xin, Farhat, Mohamed, 2021. A review of cavitation in tip-leakage flow and its control. *J. Hydrodyn.* 1–17.
- Cheng, H., Long, X., Ji, B., Peng, X., Farhat, M., 2020. A new Euler-Lagrangian cavitation model for tip-vortex cavitation with the effect of non-condensable gas. *Int. J. Multiph. Flow* 134, 103441.
- Coleman, Hugh W., Steele, W. Glenn, 2018. *Experimentation, Validation, and Uncertainty Analysis for Engineers*. John Wiley & Sons.
- Crank, J., 1979. *The Mathematics of Diffusion*. Oxford University Press.
- Cussler, E.L., 2009. *Diffusion: Mass Transfer in Fluid Systems*. Cambridge University Press.
- Dreyer, M., Decaix, J., Münch-Alligné, C., Farhat, M., 2014. Mind the gap: a new insight into the tip leakage vortex using stereo-PIV. *Exp. Fluids* 55 (11), 1–13.
- Duarte, C.M., Chapuis, L., Collin, S.P., Costa, D.P., Devassy, R.P., Eguiluz, V.M., Erbe, C., Gordon, T.A.C., Halpern, B.S., Harding, H.R., et al., 2021. The soundscape of the anthropocene ocean. *Science* 371 (6529).
- Duncan, P.B., Needham, D., 2004. Test of the Epstein-Plesset model for gas microparticle dissolution in aqueous media: effect of surface tension and gas undersaturation in solution. *Langmuir* 20 (7), 2567–2578.
- Eller, A., Flynn, H.G., 1965. Rectified diffusion during nonlinear pulsations of cavitation bubbles. *J. Acoust. Soc. Am.* 37 (3), 493–503.
- Epstein, P.S., Plesset, M.S., 1950. On the stability of gas bubbles in liquid-gas solutions. *J. Chem. Phys.* 18 (11), 1505–1509.
- Fyrillas, M.M., Szeri, A.J., 1994. Dissolution or growth of soluble spherical oscillating bubbles. *J. Fluid Mech.* 277, 381–407.
- Gadd, G.E., Grant, S., 1965. Some experiments on cavities behind disks. *J. Fluid Mech.* 23 (4), 645–656.
- Gerz, T., Holzäpfel, F., Bryant, W., Köpp, F., Frech, M., Tafferner, A., Winkelmann, G., 2005. Research towards a wake-vortex advisory system for optimal aircraft spacing. *C. R. Phys.* 6 (4–5), 501–523.
- Groß, T.F., Pelz, P.F., 2017. Diffusion-driven nucleation from surface nuclei in hydrodynamic cavitation. *J. Fluid Mech.* 830, 138–164.
- Higuchi, H., Arndt, R.E.A., Rogers, M.F., 1989. Characteristics of tip vortex cavitation noise. *J. Fluids Eng.* 111 (4), 495–501.
- Holl, J.W., 1960. An effect of air content on the occurrence of cavitation. *J. Fluids Eng.* 82 (4), 941–945.
- Holl, J.W., Arndt, R.E.A., Billet, M.L., 1972. Limited cavitation and the related scale effects problem. In: *Second International Japanese Society of Mechanical Engineers Symposium*.
- Holl, J.W., Treaster, A.L., 1966. Cavitation hysteresis. *J. Basic Eng.* 88 (1), 199–211.
- Jones, N., 2019. Ocean uproar: saving marine life from a barrage of noise. *Nature* 568, 158–161. <http://dx.doi.org/10.1038/d41586-019-01098-6>.
- Kermeen, R.W., McGraw, J.T., 1952. *Some Observations of Cavitation on Hemispherical Head Models*. California Institute of Technology.
- Khoo, M.T., Venning, J.A., Pearce, B.W., Brandner, P.A., 2020. Statistical aspects of tip vortex cavitation inception and desinence in a nuclei depleted flow. *Exp. Fluids* 61, 1–13.
- Lecoffre, Y., Chantrel, P., Teiller, J., 1988. Le grand tunnel hydrodynamique (GTH). *La Houille Blanche* (7–8), 585–592.
- Lee, I., Mäkiharju, S.A., Ganesh, H., Ceccio, S.L., 2016. Scaling of gas diffusion into limited partial cavities. *J. Fluids Eng.* 138 (5).
- McCormick, Jr., B.W., 1962. On cavitation produced by a vortex trailing from a lifting surface. *J. Basic Eng.* 84 (3), 369–378.
- Oweis, G.F., Van der Hout, I.E., Iyer, C., Tryggvason, G., Ceccio, S.L., 2005. Capture and inception of bubbles near line vortices. *Phys. Fluids* 17 (2), 022105.
- Parkin, B., Ravindra, K., 1991. Convective gaseous diffusion in steady axisymmetric cavity flows. *J. Fluids Eng.* 113 (2), 285–289.
- Pennings, P.C., 2016. *Dynamics of Vortex Cavitation* (Ph.D. thesis). Delft University of Technology.
- Pennings, P., Bosschers, J., Van Terwisga, T., 2014. Dynamics of isolated tip vortex cavitation. In: *APS Meeting Abstracts*.
- Pennings, P.C., Bosschers, J., Westerweel, J., Van Terwisga, T.J.C., 2015. Dynamics of isolated vortex cavitation. *J. Fluid Mech.* 778, 288–313.
- Schnerr, G.H., Sauer, J., 2001. Physical and numerical modeling of unsteady cavitation dynamics. In: *Fourth International Conference on Multiphase Flow*. ICMF New Orleans.
- Soloff, Steven M., Adrian, Ronald J., Liu, Zi-Chao, 1997. Distortion compensation for generalized stereoscopic particle image velocimetry. *Meas. Sci. Technol.* 8 (12), 1441.
- Van Wijngaarden, L., 1967. On the growth of small cavitation bubbles by convective diffusion. *Int. J. Heat Mass Transfer* 10 (2), 127–134.
- van Wijngaarden, E., Bosschers, J., Kuiper, G., 2005. Aspects of the cavitating propeller tip vortex as a source of inboard noise and vibration. In: *ASME 2005 Fluids Engineering Division Summer Meeting*. American Society of Mechanical Engineers Digital Collection, pp. 539–544.
- Yu, P.W., Ceccio, S.L., 1997. Diffusion induced bubble populations downstream of a partial cavity. *J. Fluids Eng.* 119 (4), 782–787.
- Zhang, Ling-xin, Chen, Lin-ya, Peng, Xiao-xing, Shao, Xue-ming, 2017. The effect of water quality on tip vortex cavitation inception. *J. Hydrodyn. Ser. B* 29 (6), 954–961.